

Instability of a transverse liquid rivulet on an inclined plane

Javier A. Diez, Alejandro G. González
*Instituto de Física Arroyo Seco, Universidad Nacional del Centro
de la Provincia de Buenos Aires, Pinto 399, 7000, Tandil, Argentina*

Lou Kondic
*Department of Mathematical Sciences
Center for Applied Mathematics and Statistics
New Jersey Institute of Technology, Newark, NJ 07102*

This work concentrates on the stability of a viscous liquid rivulet positioned across an inclined plane under partial wetting conditions. The study is performed within the framework of lubrication approximation by employing a slip model. Both normal and parallel components of gravity are considered. We find the stability regions for given area of the cross section of the rivulet, A , plane inclination angle, α , and static contact angle, θ_0 , characterizing the wettability of the substrate. For α 's smaller than some critical angle, α^* , a static solution exists. This solution is characterized by rear/front contact angles given by $\theta_0 \pm \delta$. The linear stability analysis of this solution is performed using an efficient pseudo-spectral Chebyshev method. We analyze the effects of A , θ_0 and α on the predictions of the model, such as the dominant wavelength, the maximum growth rate and the behavior of most unstable perturbation mode. To verify the predictions, we also carry out experiments with silicone oils spreading on a coated glass substrate for a number of different fluid volumes and inclination angles. We find very good agreement between the wavelength of maximum growth rate given by the theory and the average distance between the drops after rivulet breakup. An analysis of finite size effects allows to show that inclusion of normal gravity effects leads to better agreement between theoretical and experimental results.

I. INTRODUCTION

Contact line instabilities are ubiquitous in nature, and they give place to non uniform liquid structures on solid surfaces. The most common structures are either elongated rivulets (fingers) or drops [1]. Consequently, it is necessary to study these instabilities when producing coated surfaces for applications. The interest can be focused either on the formation of very uniform coatings or on the generation of patterns. In the first case, the aim is to quench the instability and then completely wetting liquids are used. In the second case, the instability is exploited to form a desirable stable pattern, so that partially wetting liquids are employed. Here, the natural instability of contact lines is the mechanism that drives the morphological transition yielding the final pattern.

Within the attempts to analyze the uniformity of coatings produced by gravity driven spreading films, significant progress was reached in the pioneer work of Huppert [2], who studied the stability of the leading front. Several studies followed, considering both complete [1, 3–5] and partial [6–10] wetting conditions, naming just a few works here. More recently, additional works have proposed alternative models discussing relaxation of contact line in Landau-Levich geometry; see [11] and the references therein. The reader is also referred to excellent reviews discussing in detail stability of thin films in various settings [1, 12].

One of the simplest structures forming an array of aligned drops is that of a rivulet positioned on a horizontal substrate [13–16]. The linear stability analysis of this problem has been recently carried out in [17], where

a van der Waals (vdW) potential is used to account for the partial wetting conditions. Recent experimental work has shown the possibility of generating fairly regular patterns of drops by the spontaneous breakup. This has been achieved both in the macro- [18] (submillimetric) and nano- [19–22] scales. Here, we aim to study the effect of an additional force parallel to the substrate on this instability, as it is the case when the plane is inclined in a gravitational field. A pioneer work on this problem was done by Hocking & Miksis [23], who studied it within the lubrication approximation theory and employing a slip model to relax the singularity at the moving contact lines. They considered only the gravity component parallel to the plane, and ignored the normal component. We show that their approach is appropriate for small values of the cross section of the rivulet, A ; however, for larger A 's, the effect of the normal component of gravity is found to be considerable.

In this work, we use a slip model rather than a disjoining pressure one, which we employed to analyze the problem of instability development for rivulets on horizontal substrates [17, 19, 20]. The motivation is the fact that slip model combined with contact angle hysteresis supports a static solution even on inclined surfaces, what is not the case for the disjoining pressure approach, where there is always flow down the incline in the contact line region. The fact that a static solution can be explicitly found simplifies the analysis considerably, and allows for additional insight. An alternative approach was considered by a few groups [8–10], where a disjoining pressure model was employed in a dynamic setting to analyze the same configuration.

This paper is organized as follows. In Section II we introduce the problem and discuss the main properties of the base solution, including the criteria for its existence. Section III describes the slip model used to analyze the stability properties of the rivulet. The linear stability analysis of the base state, done by using a pseudo-spectral method, is presented in Section IV, which includes a marginal stability analysis, a parametric study of the dispersion relation, and the effect of the inclination angle on the shape of the perturbation modes. In Section V we report experimental results for the distance between drops that form due to rivulet breakup and compare them with the wavelength of maximum growth predicted by the theory. Finally, we summarize the main results in Section VI, and discuss the relation with the vdW model for the horizontal plane in the Appendix.

II. BASE STATIC SOLUTION

The governing equation for the thickness profile of the static rivulet, $h_0(x)$, can be obtained, for instance, by considering the fact that velocity field vanishes. Therefore, the dimensionless balance between the pressure and gravitational forces can be written as,

$$0 = -\nabla p + \hat{\mathbf{x}}F - \hat{\mathbf{z}}G. \quad (1)$$

Figure 1 shows the geometry of the problem with $\hat{\mathbf{z}}$ pointing out of the plane. The constants $F = \sin \alpha$ and $G = \cos \alpha$ account for the normal and parallel components of gravity, respectively. Here, the spatial variables are in units of capillary length $a = \sqrt{\gamma/(\rho g)}$, where g is the gravity, ρ is the fluid density, and pressure p is in units of γ/a .

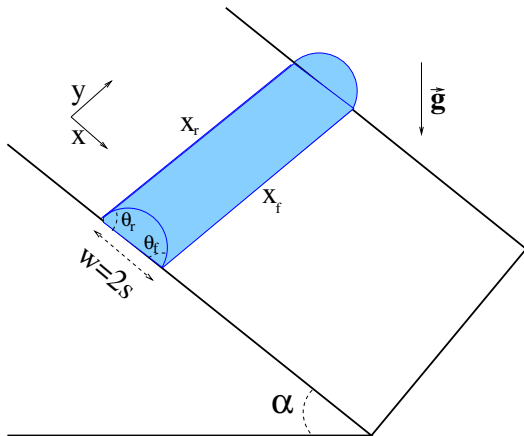


FIG. 1. Sketch of the problem. The fluid rivulet of width $w = 2s$ rests on a plane substrate inclined at angle α with respect to the horizontal under partial wetting conditions.

By introducing the surface tension boundary condition for small slopes of the free surface, $p = -h_0''$ at $z = h_0(x)$, integration of Eq. (1) yields

$$h_0'' - Gh_0 + Fx + p_0 = 0, \quad (2)$$

where the constant, p_0 , is the value of the fluid pressure inside the rivulet. The boundary conditions for Eq. (2) are

$$h_0 = 0, \quad h_0' = \tan \theta_r \quad \text{at} \quad x = x_{r,0}, \quad (3)$$

$$h_0 = 0, \quad h_0' = -\tan \theta_f \quad \text{at} \quad x = x_{f,0}, \quad (4)$$

where $x_{f,0}$ and $x_{r,0}$ are the positions of the leading (front) and trailing (rear) contact lines of the static rivulet. As shown in Section II A, two different contact angles are required to allow for mechanical equilibrium in the direction parallel to the plate. This fact implies that we must consider a hysteretic substrate which is characterized by an advancing and a receding static angle, θ_{adv} and θ_{rec} , respectively. In most practical situations, one will have $\theta_f < \theta_{adv}$ and $\theta_r > \theta_{rec}$, so that when one places a drop on an inclined substrate, both contact lines relax until equilibrium is reached.

Here, we choose $x = 0$ as the middle point of the rivulet so that $x = x_{r,0} = -s$ and $x = x_{f,0} = s$ where $s = w/2$ and w is the rivulet width. The solution of Eq. (2) which satisfies Eq. (4) can be found analytically as

$$h_0(x) = \frac{p_0}{G} \left[1 - \frac{\cosh(\sqrt{G}x)}{\cosh(\sqrt{G}s)} \right] + \frac{F}{G} \left[x - s \frac{\sinh(\sqrt{G}x)}{\sinh(\sqrt{G}s)} \right]. \quad (5)$$

The first term, which corresponds to the case of a horizontal plane, is known in the literature (see e.g. [24]), while the second term due to the inclination of the plane is new in this form. The pressure p_0 is obtained from the condition of constant area cross section

$$A = \int_{-s}^s h_0(x) dx \quad (6)$$

as

$$p_0 = \frac{A}{2} \frac{G^{3/2}}{\sqrt{G}s - \tanh(\sqrt{G}s)}. \quad (7)$$

In order to find s , we employ the contact angle conditions, Eq. (4), so that we obtain

$$\tan \theta_f = P(s) + Q(s), \quad \tan \theta_r = P(s) - Q(s), \quad (8)$$

where

$$P(s) = \frac{p_0}{\sqrt{G}} \tanh(\sqrt{G}s), \quad (9)$$

$$Q(s) = \frac{F}{G} \left[\frac{\sqrt{G}s}{\tanh(\sqrt{G}s)} - 1 \right]. \quad (10)$$

Equation (8) shows that the front and rear contact angles increases and decreases, respectively, by the same amount

$$\tan \delta = Q(s), \quad (11)$$

with respect to the average value

$$\tan \theta_0 = P(s). \quad (12)$$

Since $Q(s) = 0$ for the horizontal plane ($\alpha = F = 0$), we consider θ_0 as the static contact angle. The other input parameters are the cross sectional area of the rivulet, A , and the inclination angle, α . The corresponding value of s can be obtained from Eqs. (12), which we write as (see Eqs. (7) and (9))

$$\frac{2 \tan \theta_0}{A} = \frac{G \tanh(\sqrt{G}s)}{\sqrt{G}s - \tanh(\sqrt{G}s)}, \quad (13)$$

and solve numerically for s with given values of A and θ_0 . One also finds

$$\tan \delta = \frac{A \sin \alpha}{2 \tan \theta_0}, \quad (14)$$

giving the contact angle deviation in terms of the parameters of the problem. As expected, δ increases as the substrate becomes more inclined, as well as for larger cross sections. This equation also shows that larger δ is required for equilibrium for fluids which better wet the surface (smaller θ_0). We note that, consistently with our previous works, we keep factors such as $\tan \theta_0$ without approximating $\tan \theta_0 \approx \theta_0$ although strictly speaking lubrication is valid only for small contact angles.

A. Existence condition for the base solution

So far, the basic (static) solution seems to be completely determined for given values of A , θ_0 and α . However, the receding contact angle cannot be less than θ_{rcd} . For lower angles, the hysteresis at the contact line no longer sustains a static solution. Therefore, we obtain the limiting condition $\tan \delta_{max} \leq \tan \theta_0 - \tan \theta_{rcd}$ (see Eqs. (8)-(12)). From Eq. (14), we find the maximum inclination angle for the liquid rivulet to be at rest as

$$\sin \alpha^* = \frac{2 \tan \theta_0 \tan \delta_{max}}{A}. \quad (15)$$

This expression implies that $\alpha^* \leq \pi/2$ for $A \geq 2 \tan \theta_0 \tan \delta_{max}$, and that $\alpha^* = \pi/2$ otherwise. Therefore, for $\alpha > \alpha^*$ the front and/or rear contact lines start to move downhill since static solution does not exist. Earlier work on this topic [23] did not discuss this critical angle, since it was only concerned with $A \ll 1$ and then $\alpha^* = \pi/2$. Equation (15) was also obtained and verified experimentally for drops on inclined planes [25, 26].

Figure 2a shows how α^* varies with A for some values of the static contact angle, θ_0 , considering the maximum hysteretic effect, i.e. for $\theta_{rcd} = 0^\circ$. As mentioned above, $\alpha^* = \pi/2$ for A smaller than a certain limit, so that a thin enough rivulet will remain in place even for a vertical plane. For sufficiently large A , α^* is a decreasing function of A , since the thicker the rivulet, the smaller is the inclination angle needed to make it slide down. Thus, the effect of increasing θ_0 is to increase α^* for a given area. The role played by a more realistic hysteresis, i.e. for

$\theta_{rcd} > 0^\circ$ is shown in Fig. 2b, where we have considered a given θ_0 and a few possible values of θ_{rcd} . We then see that a main effect of reducing hysteresis is to decrease α^* from its maximum value, α_{max}^* , for $\theta_{rcd} = 0^\circ$ (solid curve in Fig. 2b). For fixed α , we find the critical cross section of the rivulet,

$$A^* = \frac{2 \tan \theta_0 \tan \delta_{max}}{\sin \alpha}, \quad (16)$$

so that the static solution does not exist for $A > A^*$. Since A^* is a decreasing function of θ_{rcd} , we define A_{max}^* as the one for $\theta_{rcd} = 0^\circ$.

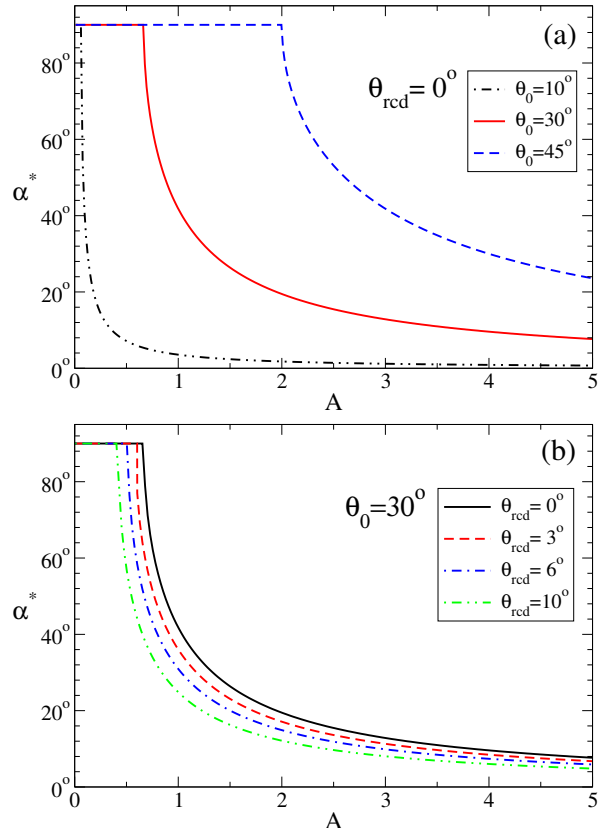


FIG. 2. Maximum inclination angle, α^* , for the rivulet at rest as a function of the cross section, A : (a) for different values of θ_0 and maximum hysteresis effect ($\theta_{rcd} = 0^\circ$), and (b) for different values of the minimum receding angle, θ_{rcd} , and given θ_0 .

It should be mentioned that some of the reported results can be obtained from simple physical considerations, without the need for an analytical solution for the thickness profile. For instance, we can start from the equilibrium condition

$$A \sin \alpha = \cos \theta_f - \cos \theta_r, \quad (17)$$

which states that the net force at the contact lines balances the rivulet weight. From this equation one can extract the deviation angle, δ , by inserting Eq. (8), and using a small θ_0 approximation. Moreover, α^* (for a given

value of θ_{rcd}) can also be obtained from energetic considerations as follows. At the onset of the rivulet movement, the flow will start only when the work of the gravitational force is greater than or equal to the work of adhering forces, so that at this critical condition we have

$$\Delta E dx = \gamma A \sin \alpha^* dx, \quad (18)$$

where dx is a virtual displacement of the contact lines, and $\Delta E = \Delta E_r + \Delta E_f$ is the variation of the (dimensional) surface energy at the rear and front boundaries. Considering different free surface angles at both contact lines (namely, θ_r and θ_f), and the energies before and after the virtual motion, the variations of the surface energy are given by

$$\Delta E_r = \gamma_{SG} - \frac{\gamma}{\cos \theta_r} - \gamma_{SL}, \quad (19)$$

$$\Delta E_f = \gamma_{SL} + \frac{\gamma}{\cos \theta_f} - \gamma_{SG}, \quad (20)$$

where the subscripts G , L and S refer to the ambient gas, liquid and solid substrate, respectively. Here, the terms on the right hand side are related to the gain or loss of surface due to the virtual motion, so that the second term refers to the free surface $dx/\cos\theta$, and the first and third ones to the SG and SL surfaces. Thus,

$$\Delta E = \gamma \left(\frac{1}{\cos \theta_f} - \frac{1}{\cos \theta_r} \right). \quad (21)$$

Then, by replacing this expression in Eq. (18) and assuming $\theta_0 \ll 1$, we obtain Eq. (15) again.

B. Properties of the basic solution

For $A \ll 1$, and given contact angle θ_0 , we expect also small values of s . Thus, we expand Eq. (13) in terms of s for $s \ll 1$, to find to the leading order

$$s \approx s_0 = \sqrt{\frac{3A}{2 \tan \theta_0}}, \quad (22)$$

Note that, in this limit, s_0 turns out to be independent of the plane inclination angle, α . A similar expansion of Eq. (7) gives the pressure inside the rivulet as $p_0 \approx 3A/(2s_0^3)$, so that the thickness profile in Eq. (5) for $s \ll 1$ becomes [23]

$$h_0(x) \approx \frac{3A}{4s_0} \left(1 + \frac{AF}{2 \tan^2 \theta_0} \frac{x}{s_0} \right) \left(1 - \frac{x^2}{s_0^2} \right). \quad (23)$$

The leading order terms for the contact angles of this profile are given by Eq. (8) as

$$\tan \theta_r \approx \frac{3A}{2s_0^2} - \frac{Fs_0^2}{3}, \quad \tan \theta_f \approx \frac{3A}{2s_0^2} + \frac{Fs_0^2}{3}, \quad (24)$$

where the first term corresponds to $\tan \theta_0$, and the second one to $\tan \delta$ (see Eq. (8)). Note that the parameter

$AF/(2 \tan^2 \theta_0)$ in Eq. (23) is equal to $\tan \delta / \tan \theta_0 \leq 1$ for $\alpha < \alpha^*$. We also observe that G does not appear in the above equations, so that the limit $A \ll 1$ can be considered as the solution for negligible normal component of gravity, which is in fact the problem studied earlier [23].

For large values of A , and within the range $0 \leq \alpha < \alpha^*$, the rivulet width $w = 2s$ is calculated from Eq. (13). Figure 3 shows w as a function of α for $\theta_0 = 30^\circ$ and different A 's. The first order solution (without normal gravity effects) is also shown for comparison as dashed lines. Due to the flattening effect of normal gravity, $w > w_0 = 2s_0$. The normal component of gravity can be safely neglected only for small values of A – e.g., the difference is about 4% for $A = 0.5$ at $\alpha = 0$.

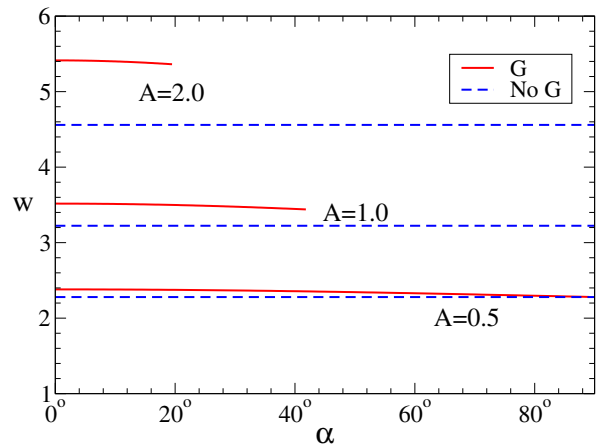


FIG. 3. Width of the rivulet as a function of the plane inclination, $\alpha < \alpha_{max}^*$, for $\theta_0 = 30^\circ$ and different cross sections, A . The solid and dotted lines show the width from Eq. (13) and the approximation, w_0 , from Eq. (22) (without normal gravity effects), respectively.

To illustrate the shape of the static rivulet solution, Fig. 4 shows the thickness profiles for $A = 1$, $\theta_0 = 30^\circ$ and several values of $\alpha < \alpha^* = 41.8^\circ$. Figure 5 shows a comparison between the profiles with and without normal gravity effects where the flattening effect due to gravity is clearly seen.

III. SLIP MODEL

Considering stability of the rivulet leads to the issue of moving contact lines. Here, we resort to the slip model to regularize the well known singularity there [27]. In this context, instead of the no-slip condition of zero velocity parallel to the substrate, i.e. $v_x = 0$ at $z = 0$, the Navier boundary condition

$$v_x = \frac{\tilde{\ell}}{3} \frac{\partial v_x}{\partial z} \quad (25)$$

is used at $z = 0$ to allow the fluid to slip on the substrate, where $\tilde{\ell}$ is the slipping length. Therefore, under

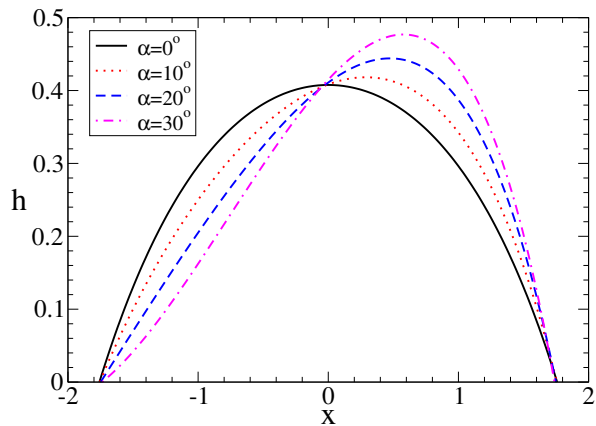


FIG. 4. Thickness profiles (base solutions) for $A = 1$ and $\theta_0 = 30^\circ$ for different values of $\alpha < \alpha^* = 41.8^\circ$.

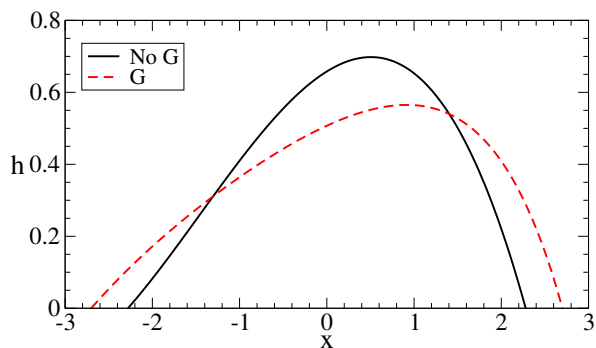


FIG. 5. Thickness profiles (base solutions) for $A = 2$, $\theta_0 = 30^\circ$, and $\alpha = 10^\circ$ with and without normal gravity effects.

the usual assumptions of the lubrication theory, the governing equation for the thickness $h(x, y, t)$ obeys the following *dimensionless* fourth order nonlinear partial differential equation [23, 28]

$$\frac{\partial h}{\partial t} + \nabla \cdot [h^2(h + \ell)\nabla(\nabla^2 h - Gh)] + F \frac{\partial}{\partial x} [h^2(h + \ell)] = 0, \quad (26)$$

where $\ell = \tilde{\ell}/a$, and time t is in units of $3\mu a/\gamma$. The conditions at the boundaries (contact lines) of the rivulet are now

$$h = 0, \quad \text{at } x = x_r(y, t), x_f(y, t), \quad (27)$$

where x_f and x_r are the positions of the leading (front) and trailing (rear) boundary of the rivulet. Since the initially straight contact lines may become corrugated during the drop motion, the slopes at the front and back boundaries are given by

$$-\left. \frac{\partial h}{\partial x} \right|_{x=x_f} \left[1 + \left(\frac{\partial x_f}{\partial y} \right)^2 \right]^{-1/2} = \tan \theta_f, \\ \left. \frac{\partial h}{\partial x} \right|_{x=x_r} \left[1 + \left(\frac{\partial x_r}{\partial y} \right)^2 \right]^{-1/2} = \tan \theta_r, \quad (28)$$

where we assume that the amplitude of the corrugation is small, so that $\partial h/\partial y \ll 1$. Note that by putting $\ell = 0$, and ignoring y and t dependence in Eqs. (26), (27) and (28), we recover the equations describing the static solution, $h_0(x)$.

IV. LINEAR STABILITY ANALYSIS

In order to analyze the linear stability of the equilibrium static solution obtained in Section III, we perform a linear modal analysis of Eq. (26). Thus, we perturb the thickness $h(x, y, t)$ and the positions of the rivulet contact lines with undulations of wavelength λ along the rivulet as

$$h(x, y, t) = h_0(x) + \epsilon g(x) \cos(qy) e^{\omega t}, \quad (29)$$

$$x_f(y, t) = s + \epsilon \xi_f \cos(qy) e^{\omega t}, \quad (30)$$

$$x_r(y, t) = -s + \epsilon \xi_r \cos(qy) e^{\omega t}, \quad (31)$$

where $q = 2\pi/\lambda$ is the wavenumber. Substituting Eq. (29) into Eq. (26), we formulate the following eigenvalue problem

$$\mathcal{L}g = -\omega g. \quad (32)$$

Here, \mathcal{L} is a linear operator defined in compact form by

$$\mathcal{L}g = H_0(D^2 - q^2)(D^2 - q^2 - G)g + DH_0(D^2 - q^2 - G)Dg, \quad (33)$$

where $D = d/dx$ and $H_0 = h_0^2(h_0 + \ell)$. This expression can be expanded as

$$\mathcal{L}g = c_4(x)g_{xxxx} + c_3(x)g_{xxx} + c_2(x)g_{xx} + c_1(x)g_x + c_0(x)g, \quad (34)$$

where the coefficients $c_i(x)$ ($i = 0, \dots, 4$) are given by

$$c_4(x) = H_0, \\ c_3(x) = DH_0, \\ c_2(x) = -(G + 2q^2)H_0, \\ c_1(x) = -(G + q^2)DH_0, \\ c_0(x) = q^2(G + q^2)H_0. \quad (35)$$

The linearized forms of the boundary conditions Eqs. (27) and (28) yield

$$g(-s) + \xi_r h_0'(-s) = 0, \xi_r h_0''(-s) + g'(-s) = 0, \quad (36)$$

$$g(s) + \xi_f h_0'(s) = 0, -\xi_f h_0''(s) - g'(s) = 0. \quad (37)$$

From the known values of the derivatives of h_0 at the boundaries, the unknown amplitudes, ξ_f and ξ_r can be eliminated from these four conditions, which are replaced by the following pair of expressions

$$g'(-s) = \frac{h_0''(-s)}{h_0'(-s)}g(-s) = \kappa^- g(-s), \quad (38)$$

$$g'(s) = \frac{h_0''(s)}{h_0'(s)}g(s) = \kappa^+ g(s), \quad (39)$$

where the constants κ^+ and κ^- depend on s as

$$\kappa^+ = \frac{Fs + p(s)}{P(s) + Q(s)}, \quad \kappa^- = \frac{Fs - p(s)}{P(s) - Q(s)}. \quad (40)$$

These boundary conditions now allow to solve the eigenvalue problem, Eq. (32), and find the eigenvalues, ω . Although the equation to be solved is linear, it is fourth order with variable coefficients, so that its solution can only be found by resorting to numerical techniques. The corresponding results are given in Section IV B; prior to describing them, we discuss the marginal stability of the problem.

A. Marginal stability

Here we discuss the boundary between the linearly stable ($\omega < 0$) and linearly unstable ($\omega > 0$) regions in the parameter space specified by (α, q) .

The neutral solution of Eq. (32) with $\omega = 0$ satisfies $(D^2 - q_c^2 - G)g = 0$ (see Eq. (34)), giving the following eigenfunction corresponding to marginally stable state

$$g(x) = C_1 \cosh \tilde{q}_c x + C_2 \sinh \tilde{q}_c x, \quad (41)$$

where $\tilde{q}_c = \sqrt{q_c^2 + G}$. Note that, as expected, this solution does not depend on the slip length, ℓ , since no motion of the contact line is required to describe the marginal stability. By inserting this expression into the boundary conditions, Eqs. (38) and (39), we obtain a system of equations for C_1 and C_2 . Since the eigenfunctions are unknown up to a multiplicative constant, we take $C_1 = 1$ and, by eliminating C_2 , we have

$$(\kappa^- - \kappa^+) \tilde{q}_c = (\kappa^- \kappa^+ - \tilde{q}_c^2) \tanh(2\tilde{q}_c s). \quad (42)$$

This equation must be solved numerically for \tilde{q}_c with the values of κ^+ and κ^- given by Eq. (40). In particular, for $A \ll 1$ ($s \ll 1$), Eq. (42) can be simplified to yield analytical expression (see also [23])

$$\left(\frac{9As_0^4}{2F}\right)^2 = \frac{(1 + q_c^2 s_0^2) \tanh(2q_c s_0) - 2q_c s_0}{(9 + q_c^2 s_0^2) \tanh(2q_c s_0) - 6q_c s_0}. \quad (43)$$

Figure 6a shows the stability diagram with the stable and unstable regions bounded by the curve $q = q_c(\alpha)$ for $\alpha < \alpha^*$, obtained for $\theta_0 = 30^\circ$, $\theta_{rcd} = 0^\circ$ and different areas. For small A , the marginal curve approaches the solution given by Eq. (43), with the larger difference at $\alpha = 0$ (see 'no G' dotted line in Fig. 6). For large A , the stabilizing effect of the normal component of gravity decreases q_c (i.e., diminishes the size of the unstable region) for all α . Note, however, that by increasing A the maximum inclination angle, α^* , decreases thus giving place to a larger no-solution region. Since no equilibrium exists in this region, some other types of instabilities are possible for $\alpha > \alpha^*$. Interestingly, the shape of the curve changes strongly for large A and small α . The fact that

q_c increases with α for a given cross sectional area shows that the parallel component of gravity is a destabilizing force, which becomes more important as A increases.

In Fig. 6b, we show the effect of the hysteresis by considering non zero values of θ_{rcd} , which modify the maximum inclination angle, α^* , below which the static solution exists. This shows that the variation of the range of hysteresis only modifies the region of existence of the solution, but its general behavior and stability are governed solely by θ_0 .

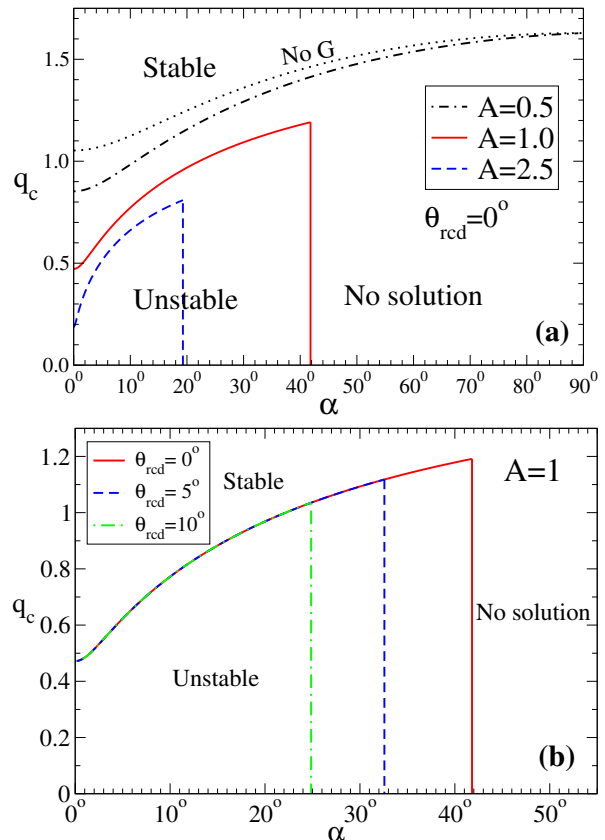


FIG. 6. Marginal stability curves in the (q, α) plane for static contact angle $\theta_0 = 30^\circ$. (a) The effect of the area, A , for $\theta_{rcd} = 0^\circ$. The dotted line 'no G' is the solution given by Eq. (43) without normal gravity effects. The rivulet is linearly stable (unstable) with respect to perturbations along the contact lines for wavenumbers above (below) the curve for the corresponding area, A . The curves end up at the corresponding α^* (vertical lines). (b) The effect of hysteresis for $A = 1$ and different values of θ_{rcd} , which show the reduction of α^* for smaller contact angle hysteresis.

In order to obtain a simplified expression for q_c in the case of a horizontal substrate, it is convenient to rewrite Eq. (42) as

$$\arg \tanh \left(\frac{\kappa^+}{\tilde{q}_c} \right) - \arg \tanh \left(\frac{\kappa^-}{\tilde{q}_c} \right) = 2\tilde{q}_c s. \quad (44)$$

Since for $\alpha = 0$ we have $\kappa^+ = -\kappa^- = \kappa$, this equation

simplifies for the horizontal case to

$$\tanh(\tilde{q}_c s) = \frac{\kappa}{\tilde{q}_c}. \quad (45)$$

By using Eqs. (9) and (40), we obtain

$$\tilde{q}_c \tanh(\tilde{q}_c s) \tanh(s) = 1, \quad (46)$$

which is coincident with Eq. (4.23) in [6], where a variational principle was used for its derivation. Therefore, Eq. (44) is a generalization to an inclined plane of the result specifying the marginal stability for the horizontal case.

As mentioned above, the marginal stability results are independent of the slip length ℓ . However, there can be influence of ℓ on the most unstable wavenumber, since instability requires front motion, see Eqs. (30) and (31) for $\omega > 0$.

B. Pseudo-spectral method

The linear eigenvalue problem posed by the differential operator in Eq. (34) combined with the boundary conditions Eqs. (38) and (39), can be solved numerically for a given value of q . This is done by discretizing the differential equation, Eq. (34), using a Chebyshev pseudo-spectral approximation of the derivatives, subject to the boundary conditions specified by Eqs. (38) and (39). This method is easier to implement and more accurate in imposing the boundary conditions at the contact lines compared to usual finite differences. Moreover, the number of nodes required with the pseudo-spectral method to obtain converged solutions is much smaller than with a difference scheme, leading to a significant reduction in the computing time (from hours to seconds).

Thus, under the pseudo-spectral method we write the solution of Eq. (34) as

$$g(x) = \sum_{i=1}^N \beta_i \phi_{i-1}(x), \quad (47)$$

where $\phi_i(x)$ is an orthogonal base and β_i are unknown spectral coefficients. By using the Gauss-Lobatto grid [29]

$$x_i = s \cos\left(\frac{\pi i}{N-1}\right), \quad i = 1, 2, \dots, (N-2), \quad (48)$$

we generate a matrix of dimension $N-2$ and require that the residual of the differential equation vanishes at the interpolation points on the interior of the interval $(-s, s)$. We allocate the remaining two rows of the N dimensional matrix to impose the boundary conditions.

In order to satisfy these conditions, we perform a basis recombination of Chebyshev functions, $T_i(x/s)$. That is, we choose a simple linear combination of the original basis functions so that the new functions individually

satisfy the boundary conditions. Thus, we use the base $\phi_i(x)$ defined by

$$\phi_i(x) = T_i(x/s) + a_i T_{i+1}(x/s) + b_i T_{i+2}(x/s), \quad (49)$$

where $T_i(x/s) = \cos(i \arccos x/s)$. By inserting $\phi_i(x)$ into Eqs. (38) and (39), we obtain two linear equations for the unknowns a_i and b_i

$$\begin{aligned} [(i+1)^2 + \tilde{\kappa}^-] a_i - [(i+2)^2 + \tilde{\kappa}^-] b_i &= \tilde{\kappa}^- + i^2 \\ [(i+1)^2 - \tilde{\kappa}^+] a_i + [(i+2)^2 - \tilde{\kappa}^+] b_i &= \tilde{\kappa}^+ - i^2 \end{aligned}$$

which are easily solved in terms of i , $\tilde{\kappa}^+ = \kappa^+ s$ and $\tilde{\kappa}^- = \kappa^- s$. Thus, we pose the eigenvalue problem

$$U_{i,j} \beta_i = -\omega V_{i,j} \beta_i, \quad i, j = 1, 2, \dots, (N-2) \quad (50)$$

where

$$U_{i,j} = \tilde{c}_4(x_i) \phi_{j-1}''''(x_i) + \tilde{c}_3(x_i) \phi_{j-1}'''(x_i) + \quad (51)$$

$$\tilde{c}_2(x_i) \phi_{j-1}''(x_i) + \tilde{c}_1(x_i) \phi_{j-1}'(x_i) +$$

$$\tilde{c}_0(x_i) \phi_{j-1}(x_i),$$

$$V_{i,j} = \phi_{j-1}(x_i), \quad (52)$$

where $\tilde{c}_i = s^i c_i$. For a given q , we find the largest eigenvalue, ω_1 , with its corresponding eigenvector, β_i^1 , which yields the eigenfunction $g_1(x)$, as given by Eq. (47) for $\beta_i = \beta_i^1$. We find that a single eigenfunction correspond to each eigenvalue.

Figure 7 shows convergence of the results as N increases. Note that convergence is faster in the unstable region ($\omega_1 > 0$) compared to the stable one ($\omega_1 < 0$). This is convenient since we are mainly interested in the growth rate of unstable modes. It should also be mentioned that the earlier work [23] focuses exclusively on this range, and the calculation of the growth rates is performed by means of an iterative method, in contrast to solving the complete eigenvalue problem as done here. We have verified that the present technique accurately reproduces the results reported in [23]. Additional calculations show that numerical convergence requires larger values of N for smaller ℓ . For example, for $\ell = 10^{-5}$ a convergence similar to that of Fig. 7 is achieved for $N = 640$.

We proceed by analyzing the dispersion curves and, in particular, their noticeable change of slope in the stable region.

C. Dispersion relation and eigenfunctions

Let us first consider the simplest case of a horizontal plane ($\alpha = 0$). Figure 8 shows the two largest eigenvalues, $\omega_1(q)$ and $\omega_2(q)$, as well as the corresponding eigenfunctions for a selected value of q . Since these functions are defined up to a constant factor, we normalize them by their maximum value in the interval $[-1, 1]$ and choose the sign so that $g(s) > 0$. With this convention, $g_1(x)$

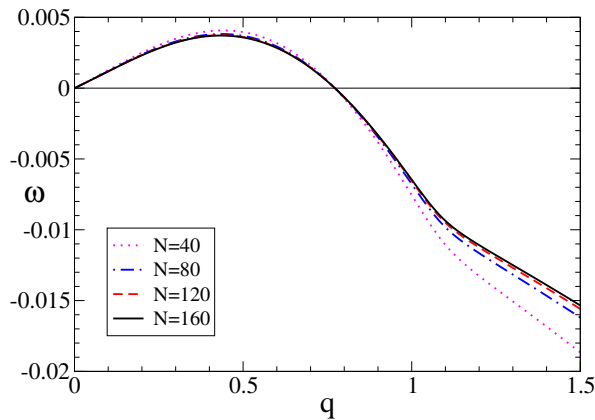


FIG. 7. Maximum eigenvalues obtained with Chebyshev pseudo spectral method versus wavenumber, q , for $\alpha = 10^\circ$ with increasing number of spectral terms, showing convergence of the results. The other parameters are as in Fig. 4.

and $g_2(x)$ correspond to symmetric (varicose) and anti-symmetric (zig-zag) modes, respectively. These properties do not change along the corresponding branch. Note also that $|g(x)|$ always reaches maximum value at the domain boundaries.

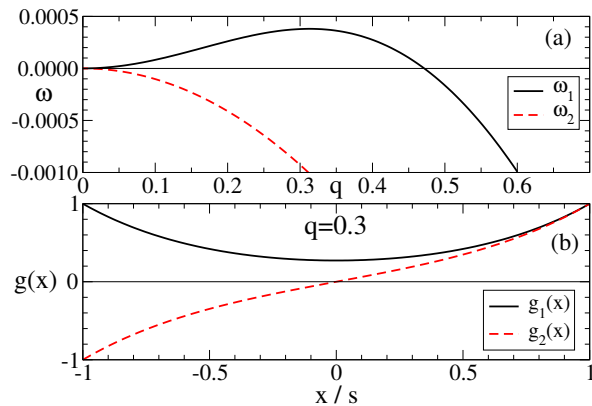


FIG. 8. (a) Dispersion curves and (b) eigenfunctions at $q = 0.3$ for the horizontal plane. The parameters are as in Fig. 4.

Next we consider the general case of an inclined plane, concentrating on the range of α 's where a static solution exists. Figure 9 shows the two largest eigenvalues, $\omega_1(q)$ and $\omega_2(q)$, for $\alpha = 10^\circ$. By comparing $\omega_1(q)$ with the results obtained for $\alpha = 0^\circ$ in the unstable region, we see that the results suggest much stronger instability (larger growth rates). It should be noted that within the present model we obtain only one maximum for the growth rate, unlike the more complex structure found in [10], where drops sliding down slightly inclined planes are described within a diffuse interface potential and without normal gravity effects.

Figure 10 shows the eigenfunctions for $\alpha = 10^\circ$. We immediately observe that the symmetry properties of the eigenfunctions are lost, so that $|g(x)|$ may be different

at both contact lines. Therefore, in the general case of an inclined plane, the modes are not strictly symmetric (varicose) nor antisymmetric (zigzag). However, if the difference $|g(s)| - |g(-s)|$ is minor, we can loosely refer to the modes as asymmetric varicose or asymmetric zigzag [9, 10]. When this difference is large (for instance, when $|g(s)| \approx 0$), this terminology may be misleading and, instead, one must pay attention to the localization of the perturbations, i.e. where the maximum value of $|g(x)|$ occurs.

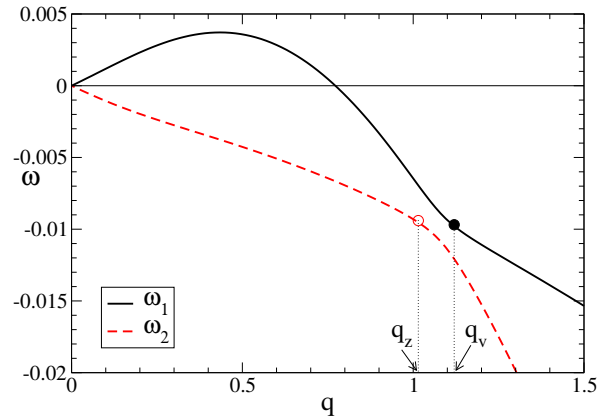


FIG. 9. First, ω_1 , and second, ω_2 , maximum eigenvalues as a function of wavenumber q for $\alpha = 10^\circ$ and $N = 160$. The solid/hollow circles point out the purely (symmetric) varicose mode, and the purely (antisymmetric) zigzag mode, respectively. The other parameters are as in Fig. 4.

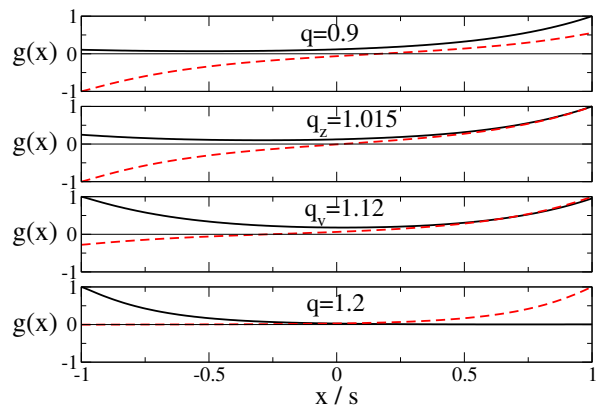


FIG. 10. Eigenfunctions $g_1(x)$ (solid lines) and $g_2(x)$ (dashed lines) of $\omega_1(q)$ and $\omega_2(q)$, respectively, for values of q before, at and after the transition region in Fig. 9.

Figure 9 shows also some perhaps more surprising results in the stable region. The curve $\omega_1(q)$ seems to be continued on $\omega_2(q)$ for $q > q_v$ (solid circle in Fig. 9). Analogously, $\omega_2(q)$ appears to be continued on $\omega_1(q)$ for $q > q_z$ (hollow circle in Fig. 9). However, we have not found a crossing of the branches in this transitional zone defined by (q_z, q_v) (to be discussed in more detail below) within a broad range of parameters of the problem, al-

though they can approach each other very closely (see also Section IV D). In other words, there is no degeneracy of the eigenvalues, and therefore $\omega_1 \neq \omega_2$ for all $q \neq 0$.

Considering now eigenfunctions for $q \in (q_z, q_v)$, we find that the behavior of $g_1(x)$ and $g_2(x)$ goes through a continuous change as q is varied. For example, $g_1(x)$ is localized predominantly at the front contact line for small q ($= 0.9$ in Fig. 10) and becomes localized at the rear one for large q ($= 1.2$ in Fig. 10). The amplitude of $g_1(x)$ is equal at both contact lines at $q_v = 1.12$, where $g_1(x)$ is a purely varicose mode. Conversely, the amplitude of $g_2(x)$ changes its localization from the rear to the front contact line as q increases, and its value is equal at both lines at $q_z = 1.015$, where $g_2(x)$ is a purely zigzag mode. Note that there is no degeneracy in the transition region (q_z, q_v), since both modes keep fixed their number of zeros as q changes (no zeros for $g_1(x)$, and one zero for $g_2(x)$). The fact that $q_v \neq q_z$ clearly indicates that the transition does not occur at a single point, but in a zone. On the other hand, if one wants to preserve the localization of the perturbation, say at the front contact line when q moves along the transition region, one must jump from $\omega_1(q)$ to $\omega_2(q)$.

Figure 11 illustrates more explicitly the evolution of eigenfunctions as q is varied. Here we characterize the eigenfunctions by the difference of their amplitudes at the boundaries

$$\Delta g_i = g_i(s) - g_i(-s). \quad (53)$$

A completely symmetric mode corresponds to $\Delta g_i = 0$, while an antisymmetric mode to $\Delta g_i = 2$. $\Delta g_i = \pm 1$ implies that there is no perturbation at one contact line, so that the mode is completely localized at the front ($\Delta g_i = 1$) or rear ($\Delta g_i = -1$). Also, note that $\Delta g_i < 1$ (> 1) means that both amplitudes have the same (different) sign.

Taking these definitions into account, Fig. 11 shows that g_1 in the unstable range ($q < q_c$) is basically localized at the front contact line. At $q \approx 0.578$ ($\Delta g_1 = 1$), there is no perturbation at the rear contact line. For $q \lesssim 0.578$ ($\Delta g_1 > 1$), the perturbation at the rear contact line is small and negative. For $q > 0.578$ ($\Delta g_1 < 1$), this perturbation is positive, and increases in size until reaching a purely antisymmetric state at $q \approx 1.12$ ($\Delta g_1 = 0$). Afterwards, $g_1(s)$ continuously decreases leading to stable modes localized at the rear contact line. The solid line in Fig. 11 shows that asymmetric zigzag modes for which $g_1(-s)g_1(s) < 0$ are expected for small q 's, while the asymmetric varicose modes are predicted for large q 's where $g_1(-s)g_1(s) > 0$. This behavior is consistent with the one described in [10].

Regarding the stable eigenfunction, g_2 , Fig. 11 shows that there are two values of q at which g_2 is purely antisymmetric ($\Delta g_2 = 2$). For $q \lesssim 0.14$, it is mainly localized at the front contact line, while the localization changes to the rear contact line for $0.14 \lesssim q \lesssim 1.015$. As q increases, the perturbation becomes more and more localized at the

front contact line again.

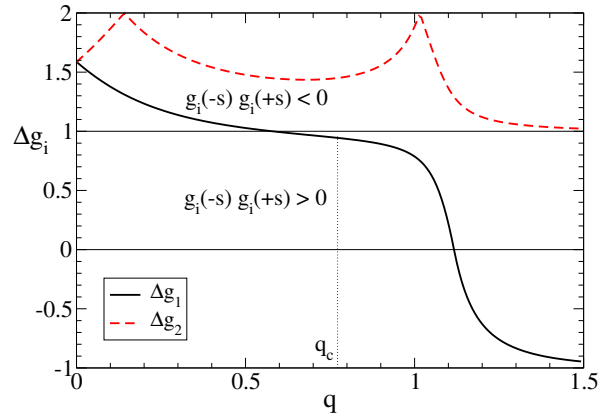


FIG. 11. Difference of amplitudes at the boundaries, Δg_i , as a function of the wavenumber q for g_1 (solid line) and g_2 (dashed line). The marginal wavenumber is denoted by q_c . The parameters are as in Fig. 9.

D. Parametric study

In this section, we study how the main features of the instability depend on the values of α , ℓ and A . Figure 12 shows the influence of α , for $\alpha < \alpha^* = 41.8^\circ$, assuming $\theta_{rcd} = 0^\circ$ (the corresponding thickness profiles of the base solutions are shown in Fig. 4). Interestingly, the change of slope of the branch $\omega_1(q)$ at $q = q_t$ is more pronounced as α approaches α^* . In the stable region, ω_1 increases for all q , so that in the limit $\alpha \rightarrow \alpha^*$, $\omega_1 \rightarrow 0$ for $q > q_c$.

Figure 13 shows, for the unstable regime, both the maximum growth rate, ω_m , and the corresponding wave number, q_m , as the plane becomes more inclined. Note that q_m doubles in size when going from the horizontal plane to α^* , while ω_m grows by a factor close to 100. Therefore, a rivulet breaks up faster into a set of smaller droplets as the substrate is inclined. We observe a qualitative agreement of $\omega_m(\alpha)$ with the results reported in [10] (Fig. 9 there).

Figure 14 shows the effect of varying ℓ for $\alpha = 10^\circ$, $A = 1$, and $\theta_0 = 30^\circ$. Here we explore the ℓ 's in the range 10^{-2} – 10^{-5} , using $N = 960$, a resolution which is sufficient to ensure convergence in this ℓ -range. The tendency of decreasing growth rates in the unstable region is in agreement with the results in [23] for $A \ll 1$. Note that the change of slope of the curves in the stable region is more pronounced for smaller ℓ . We also note here that, assuming that appropriate length scale for ℓ is of the same order as the range of intermolecular forces defining liquid/substrate interaction (1–10 nm), we find that in our nondimensional units, for the capillary length $a \approx 1$ mm, $\ell > 10^{-6}$ – 10^{-5} . This range of values gives approximate lower bound on appropriate values of ℓ .

Next we discuss the influence of cross-sectional area. Figure 15 shows $\omega_1(q)$ and $\omega_2(q)$ for increasing val-

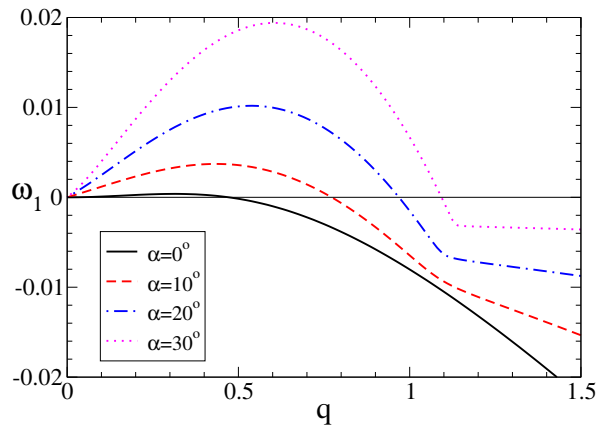


FIG. 12. Dispersion relations for $N = 160$ for different values of $\alpha < \alpha^* = 41.8^\circ$, assuming $\theta_{rcd} = 0^\circ$. The parameters are as in Fig. 4.

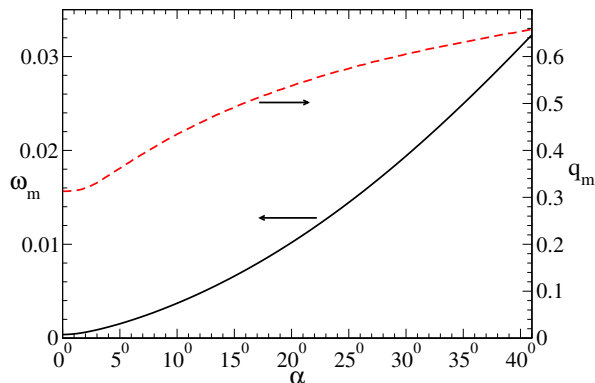


FIG. 13. Maximum growth rate, ω_m , and corresponding wave number, q_m , as function of α for the same data as in Fig. 12.

ues of A , keeping all other parameters constant. The growth rate of the most unstable wavenumber, ω_m , increases with A , and the corresponding stable region has decreasing (in absolute value) growth rates, which vanish as A approaches the critical area, $A^* = 2 \tan \theta_0 \tan \delta_{max} / \sin \alpha$. This behavior is analogous to the one seen in Fig. 12. In addition, the transition zone becomes more narrow and also $q_t \rightarrow q_c$ as $A \rightarrow A_c$. The inset in Fig. 15b, which corresponds to a zoom-in of this zone, shows that the branches do not cross, but approach each other as $A \rightarrow A^*$. Thus, for $A \approx A^*$ there is a rapid change of the dominant perturbation mode, from $g_1(x)$ to $g_2(x)$ at $q \approx q_c$. We find that $\omega_2(q)$ shows a second abrupt change of slope for $q > q_c$, see Fig. 15c for $A = 3.5$. Figure 16 shows more clearly the source of this result: there is actually a cascade of these transitions associated with $\omega_3 < \omega_2$, $\omega_4 < \omega_3$, etc. This cascade also occurs for parameters far from the critical ones, although not necessarily in such a narrow range of q 's.

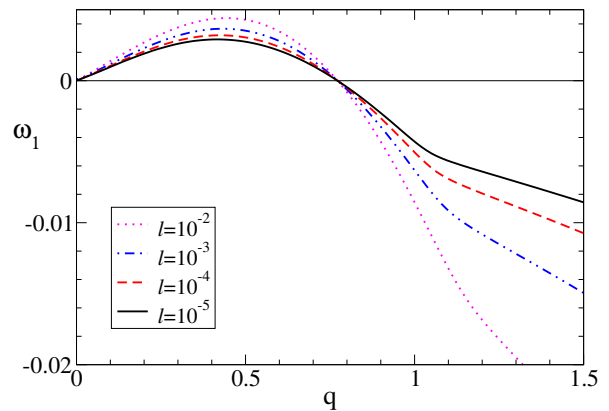


FIG. 14. Maximum eigenvalues versus wavenumber q for decreasing slip length, ℓ ; here $\alpha = 10^\circ$. All results are converged for the large value of $N = 960$ used here. The other parameters are as in Fig. 4.

E. Properties of most unstable eigenfunctions

Here, we discuss the behavior of the most unstable eigenfunctions for different $\alpha < \alpha^*$. Figure 17 shows that for the horizontal plane, the perturbation is symmetric with maxima at both contact lines, as discussed before. This symmetry is rapidly lost for $\alpha > 0$, with different behavior of the amplitudes at those lines. At the rear contact line, $g_1(-s)$ decreases and becomes negative for $\alpha > 2^\circ$, reaching a minimum value for $\alpha \approx 10^\circ$ (this particular values are consequence of the set of parameters used). For larger α , $g_1(-s)$ approaches zero from the negative side as $\alpha \rightarrow \alpha^*$. On the other hand, the amplitude at the front contact line, $g_1(s)$, is always a maximum.

The evolution of $g_1(x)$ as α is varied can also be visualized in terms of the displacements ξ_r and ξ_f at the contact lines, which are given by (see Eq. (37))

$$\begin{aligned} \xi_r &= -\frac{g(-s)}{h'_0(-s)} = -\frac{g_1(-s)}{\tan \theta_r} \\ \xi_f &= -\frac{g(s)}{h'_0(s)} = \frac{g_1(s)}{\tan \theta_f}. \end{aligned} \quad (54)$$

Figure 18 shows ξ_r and ξ_f for $\alpha < \alpha^*$. Since $g_1(s) = 1$, the variation of ξ_f is only due to the modification of θ_f as the plane is inclined. We see that ξ_f reduces to approximately half of its value at $\alpha = 0$ as α approaches α^* . On the other hand, ξ_r is governed mainly by $g_1(-s)$, which determines its decrease as $\alpha \rightarrow \alpha^*$ (the numerator in the expression for ξ_r in Eq. (54) goes to zero faster than the denominator). As a consequence, at α^* the front boundary is modulated by a finite amplitude, while the rear contact line has negligible amplitude and resembles a straight line. Note that the instability has non-zero maximum growth rate for $\alpha = \alpha^*$, where also an onset of the bulk motion is expected.

Figure 19 shows explicitly the shape change of the rear and front contact lines as α varies. Here, we plot

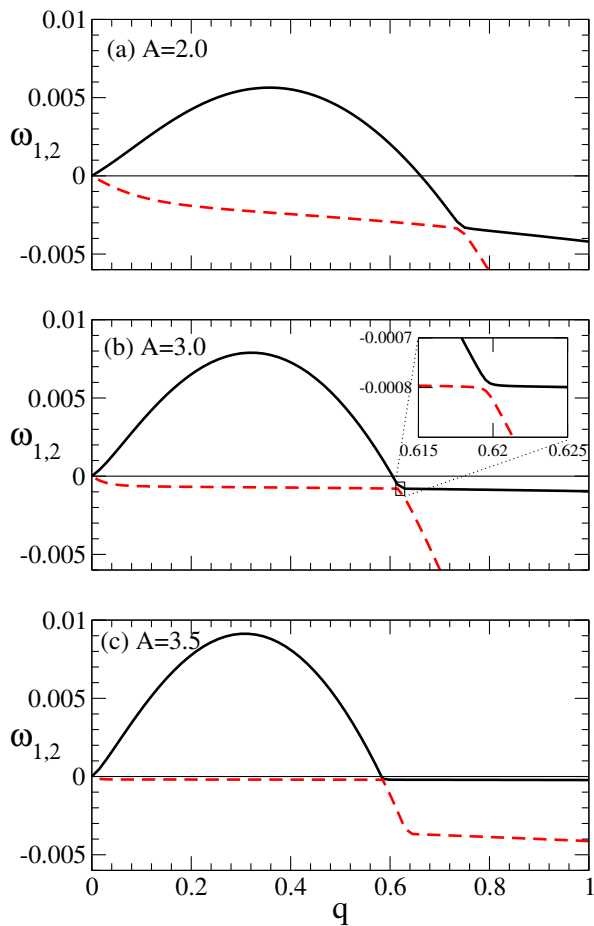


FIG. 15. First, ω_1 (solid lines), and second, ω_2 (dashed lines) largest eigenvalues as a function of wavenumber, q , for increasing values of A with $\alpha = 10^\circ$. The inset is a zoom-in of the transition zone showing that the curves do not touch each other. Here, the critical area is $A^* = 3.84$. The other parameters are as in Fig. 4.

Eqs. (30) and (31) for the corresponding values ξ_r and ξ_f and use (large) $\epsilon = 0.2$ for visualization purposes.

V. EXPERIMENTS

In order to evaluate the applicability of the linear theory presented here, we perform a series of experiments using silicon oils and glass substrates. We choose PDMS (polydimethylsiloxane) as a suitable liquid because of its almost vanishing evaporation rate, and also due to its Newtonian behavior in the range of shears of our experiments. The measured values of viscosity, surface tension and density are $\mu = 20$ g/(cm s), $\gamma = 21$ dyn/cm², and $\rho = 0.96$ g/cm³, respectively. Since PDMS wets the clean glass, we coat the substrates with a fluorinated solution (derived from EGC-1700 of 3MTM) to achieve partial wetting conditions. We employ the dip coating method (immersion and withdrawal of the substrate into the solution with controlled speed), as done in previous

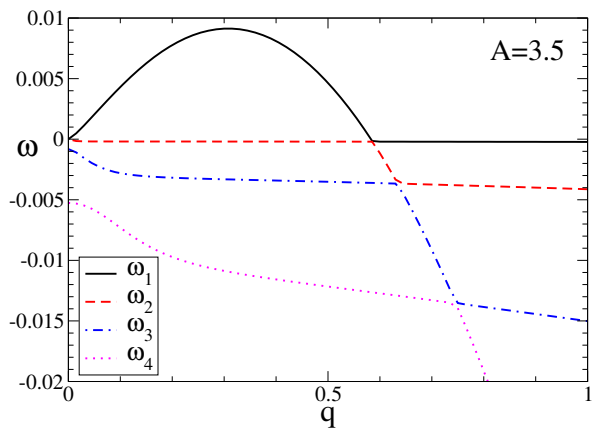


FIG. 16. Cascade of transitions for $\omega_1 > \omega_2 > \omega_3 > \omega_4$ for the case shown in Fig. 15c.

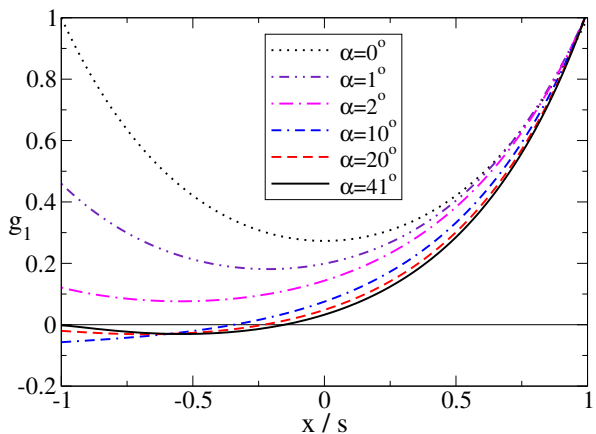


FIG. 17. Eigenfunctions for $q = q_{max}$ and different inclination angles, $\alpha < \alpha^* = 41.8^\circ$, for $\alpha = 10^\circ$. Here, we use $N = 160$. The other parameters are as in Fig. 4.

works [18]. The weight of the substrate (a microscope slide of length $\tilde{L} = 7.5$ cm (we will use ‘tilde’ to distinguish dimensional variables in this section) before and after the dipping process indicates that the thickness of the coating, after complete evaporation of the solvent, is about 1 μ m.

The rivulet is formed by a portion of a liquid jet which emerges from a vessel containing PDMS. This is accomplished by performing a series of rotational motions of the frame that holds the substrate, as described elsewhere [18]. Then, the substrate is placed at the desired angle of inclination. This procedure generates a liquid filament (rivulet) with parallel contact lines on the coated glass. The cross section of the rivulet is varied by using jets of different diameters, determined by opening of the vessel’s nozzle and the height of the liquid in the vessel.

The static contact angle of a PDMS droplet positioned on the coated substrate is measured by using a refractive technique [18] yielding $\theta_0 = 17^\circ \pm 1^\circ$. In order to quantify the hysteresis of the system, we carried out experi-

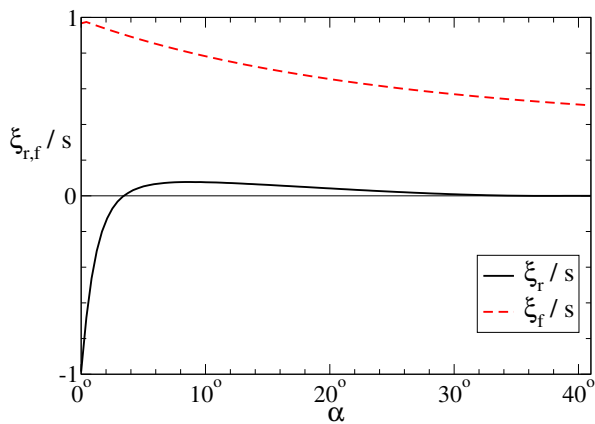


FIG. 18. Amplitudes of the contact line perturbations at the rear, ξ_r , and front, ξ_f contact lines of the rivulet (see Fig. 17 and Eq. (54)) at different plane inclination angles, $\alpha < \alpha^*$. The parameters are as in Fig. 17.

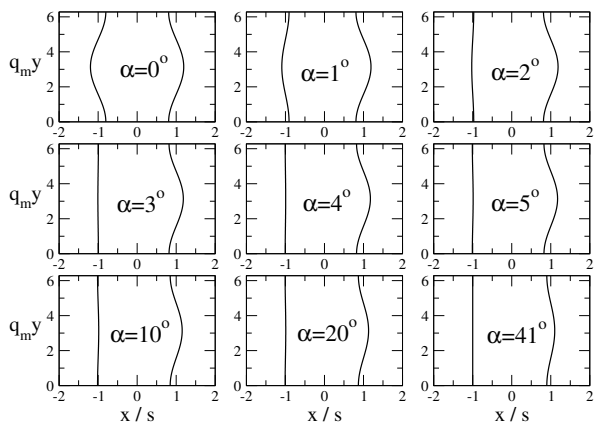


FIG. 19. Evolution of the most unstable mode perturbing both contact lines for different inclination angles, α , obtained using the data from Fig. (18) and Eqs. (30) and (31) with $t = 0$. The parameters are as in Fig. 17.

ments by continuously varying the inclination for rivulets of known cross sections. This can be done easily for relatively large A 's, which have small enough growth rates for the contact line instability for our viscous PDMS. Thus, we determine the critical angle at which the rivulet starts to slide down and, by using Eq. (15), we obtain $\theta_{rcd} = 4^\circ \pm 1^\circ$. This result is consistent with those reported by other authors (see, e.g., [30]), who also find hysteresis amplitude of the order of $\approx 10^\circ$.

We carry out experiments with several inclination angles and areas, and record the evolution of the contact lines as well as configuration of the drops that form. Figure 20 shows the final drop pattern after complete breakup of a rivulet with cross section $\tilde{A} = 0.032a^2$ on a horizontal plane (see also [18]).

Additional experiments with different A 's were carried out and averaged distance between the drops extracted. Figure 21 summarizes the results for this average dis-

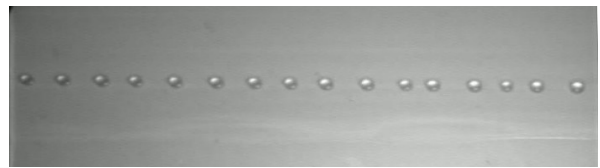


FIG. 20. Final drop configuration for a PDMS rivulet with cross section $\tilde{A} = 0.0007 \text{ cm}^2 = 0.032a^2$ on a horizontal substrate, where $\theta_0 = 16^\circ \pm 1^\circ$.

tance, shown as solid circles. These results can be now compared with the theoretical prediction from the linear stability analysis, λ_m , shown by the solid and dashed curves with and without normal gravity, respectively. Note the good agreement between the experimental data and both theoretical curves for small areas ($< 0.1a^2$). For large areas, the experiments are better fitted by the solid curve, indicating that gravity becomes important, and that its effects are accurately taken into account by the theory.

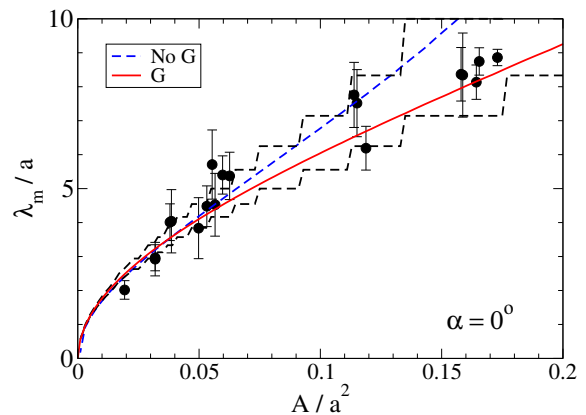


FIG. 21. Average spacing between drops (symbols) as a function of the cross section of the rivulet, A , for the horizontal case ($\alpha = 0^\circ$). The curves correspond to λ_m as predicted by the LSA considering and neglecting gravity effects, and using $\ell = 10^{-3}$. The step-like dashed lines are illustrating finite-size effects, as discussed in the text.

The dispersion of the experimental data can be understood by recalling finite rivulet lengths effects. In fact, the wavelength of the mode of maximum growth rate, λ_m , may not fit an integer number of times in the length, L , of the rivulet. Thus, the system tends to select the closest possible spacing between drops that fits in the rivulet length and yields an integer number of identical drops, n_d . By taking this into account, we define a range of expected drops spacing that can have a positive or negative difference of at least one drop with respect to L/λ_m . This leads to the following upper and lower bounds

$$(\lambda_+, \lambda_-) = \begin{cases} \left(\frac{L}{n_0}, \frac{L}{n_0+2} \right) & \text{if } n_d - n_0 > 0.5 \\ \left(\frac{L}{n_0-1}, \frac{L}{n_0+1} \right) & \text{if } n_d - n_0 < 0.5, \end{cases} \quad (55)$$

where n_0 is the integer part of L/λ_m . We apply these ideas to the model with gravity in Figure 21. The piecewise staircase function plotted there shows that most of the experimental data fall within the band of expected values of the spacing. Note that for large areas, the number of drops strongly decreases, and thus the band ($\lambda_+ - \lambda_-$) increases in size, justifying finding larger dispersion in the experiments.

We consider now a substrate with an inclination angle of $\alpha = 30^\circ$, which yields $A^* = 0.29$ (see Eq. (16)). Figure 22 shows the evolution of the instability for $\tilde{A} = 0.113a^2$. Analogously to the horizontal case [18], we observe a pearling instability propagating from the ends concomitant with the contact line instability driven by both the surface tension and the component of gravity parallel to the substrate. Both mechanisms operate simultaneously: the former producing bulges and breakups at the necks from the ends, and the latter developing corrugations. Furthermore, they lead to same distance between the drops, as discussed extensively in [17] for the horizontal rivulet case. Note that, in agreement with the theoretical results shown in Fig. 19, the rear contact line remains practically straight, while the front contact line develops corrugations.

Figure 23 shows that for a larger area, $\tilde{A} = 0.208a^2$, and the same inclination angle, one finds a similar pattern of instability, but the drops are larger and their total number is smaller. After the rivulet breaks up, some of the resulting drops slide down because of their large volume. Since the drops at the ends of the original rivulet are big enough to slide and they are formed earlier, they travel a longer distance than the central ones. Therefore, the arrangement of drops is somewhat curved. The breakup process occurs, however, along the straight rivulet where the rear contact line is practically at rest (note that the critical angle $\alpha^* = \pi/2$ for this area); for this reason we measure the distance between the drops along the original straight rivulet. Note that at some breakups satellite droplet may form (see e.g. between the third and fourth drops from the left in Fig. 23). These are not considered when measuring the average spacing between drops, since they correspond to a phenomenon on a different scale.

Figure 24 shows comparison of the average distance between the drops for $\alpha = 30^\circ$ with the theoretical prediction, λ_m . Note that the difference between the curves with and without normal gravity is smaller than for the horizontal case due to the decrease of the normal component of gravity. Within the measurement errors, the experimental data for the considered range of areas ($A < 0.2$) are in good agreement with both theoretical curves.

Figure 25 shows the details of the formation of bulges at the tips of a short filament. In an advanced nonlinear stage, a neck develops and eventually breaks up leading to the formation of two main drops as well as satellite droplets of smaller size in between. Further evidence of these droplets are reported in [18]. It should be noted

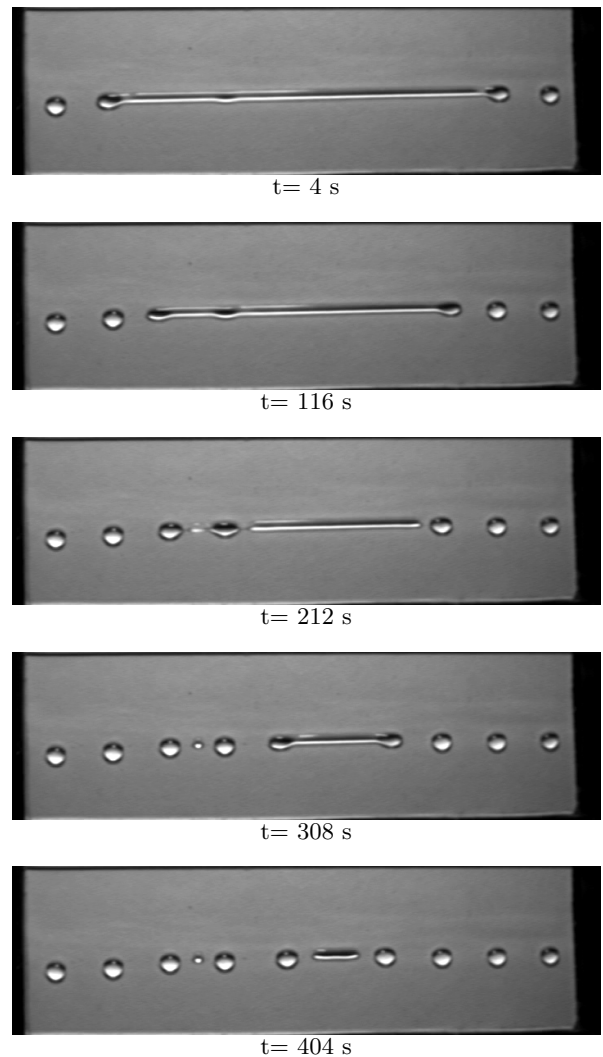


FIG. 22. Evolution of a PDMS rivulet with cross section $\tilde{A} = 0.0025 \text{ cm}^2 = 0.113a^2$. The inclination angle is $\alpha = 30^\circ$.

that the rear contact line remains straight all along the rivulet, except in this narrow region of the neck. This deviation from a straight shape can be seen only for a short time during which a breakup occurs.

Next, we consider an almost vertical case of $\alpha = 80^\circ$ ($A^* = 0.15$). Figure 26 shows the time evolution of the instability for the same area as in Fig. 22. Due to the larger inclination angle, the front contact line becomes visibly corrugated in the central part of the rivulet. This feature leads to breakups in this region simultaneously with those at the ends. As expected, the final pattern is more curved compared to the one seen for $\alpha = 30^\circ$ with the same area.

Figure 27 shows the comparison between the measured drop distance for different areas and λ_m for $\alpha = 80^\circ$. The curves with and without normal gravity are almost coincident in this case for this range of areas. The experimental data are well fitted by these curves for small A

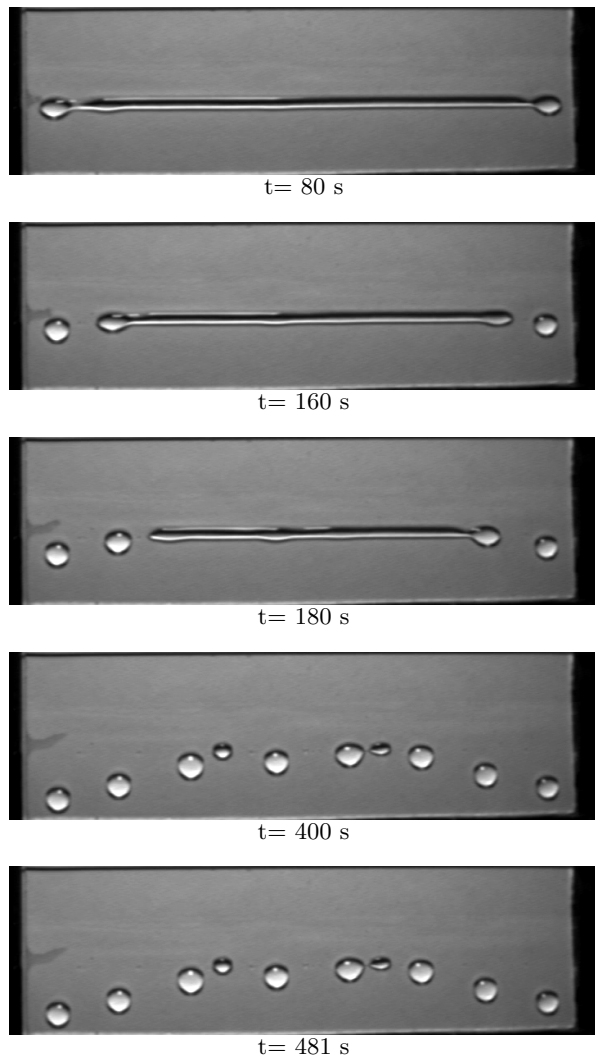


FIG. 23. Evolution of a PDMS rivulet with cross section $\bar{A} = 0.0046 \text{ cm}^2 = 0.208a^2$. The inclination angle is $\alpha = 30^\circ$.

(< 0.1), while for larger A 's the theory somewhat overestimates the spacings. We believe that this can be related to the fact that, for this large inclination, large area rivulets tend to breakup early in their central region, and then two shorter rivulets with the same A as the original one evolve independently. These shorter rivulets yield a smaller number of drops and, consequently, lead to a greater dispersion in the spacing between drops. Moreover, for $A > A^*$ one expects some departures from the theory since the rivulet should be slowly sliding down.

VI. SUMMARY AND CONCLUSIONS

In this paper we consider the problem of a liquid rivulet positioned across an inclined plane under partial wetting conditions. For a range of inclination angles, we find that there exists a base static solution, where a rivulet does

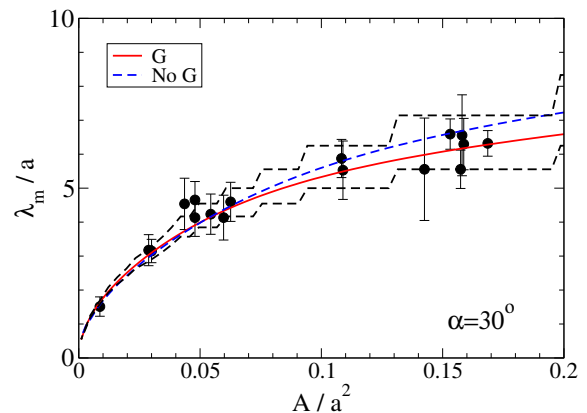


FIG. 24. Average spacing between drops (symbols) as a function of its cross section, A . The inclination angle is $\alpha = 30^\circ$. The curves correspond to λ_m as predicted by the LSA considering and neglecting gravity effects, and using $\ell = 10^{-3}$. The step-like dashed lines are illustrating finite-size effects, as discussed in the text.

not flow down the incline. Its stability is studied by analyzing perturbations of the front/back contact lines and of the fluid thickness. A marginal stability analysis allows to find the unstable regions for given values of cross sectional areas, A , contact angles, θ_0 , and inclination angles, α .

In order to carry out the linear stability analysis, we resort to a slip model. This study is done by using a Chebyshev pseudo-spectral method, which yields eigenmodes and eigenfunctions of the perturbations. Interestingly, for fixed inclination angle, the relative amplitude of the perturbations at the rear and front contact lines changes as the wavelength of the modes is varied. Therefore, the nearly varicose or zigzag character of the transverse eigenfunctions is not independent of the wavelength of the longitudinal perturbations. This is a distinctive feature of the instability on an inclined plane, not present on horizontal ones.

Of particular interest are the results concerning the behavior of the mode of maximum growth rate and its wavelength, λ_m . Therefore, we analyze the dependence of the corresponding eigenfunction and its amplitude at both contact lines on the inclination angle. We observe that, as the substrate is inclined starting from the horizontal position, the amplitude of the perturbation quickly decreases at the rear contact line, and the mode localizes at the front one. When the critical inclination is reached, the rear boundary is found to keep its straight shape while the front boundary reaches the maximum undulation. If the substrate is further inclined, we expect a displacement of the rivulet as a whole.

We also compare the theoretical predictions for λ_m with the experimentally determined distance between drops after the rivulet breakup. The experiments are conducted by using PDMS on coated glass under partial wetting conditions. We find a very good agreement between the experimental data and the theory for a wide

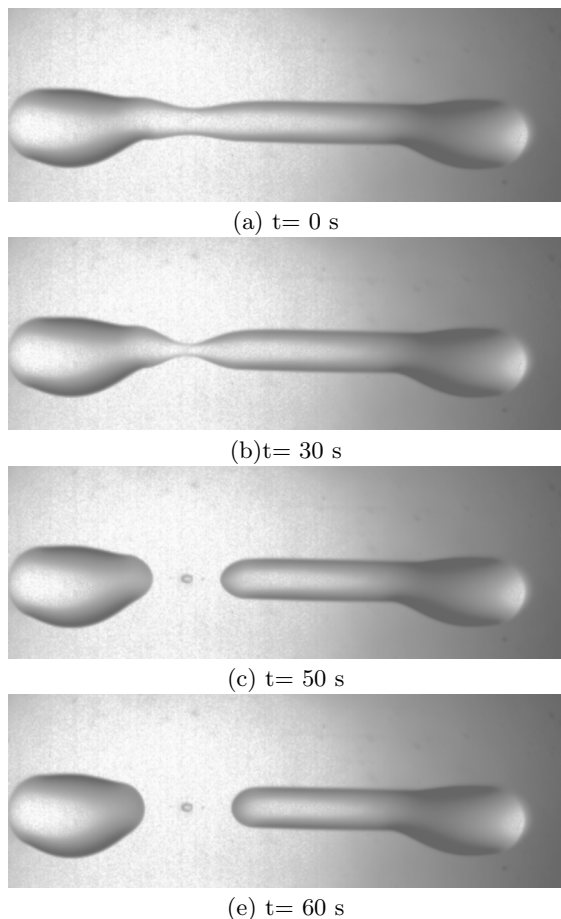


FIG. 25. Breakup of a PDMS rivulet of cross section $\tilde{A} = 0.0011 \text{ cm}^2 = 0.048a^2$, with $\alpha = 30^\circ$.

range of inclination angles, from horizontal to almost vertical. Even for α and A are large, λ_m still provides a reasonable estimate (see e.g. Fig. 27). The experiments show that for small inclination angles, it is important to include the corrections due to normal component of gravity for $A > 0.1a^2$. This finding becomes more obvious when considering finite size effects. For large α , both experiments and theory show that normal component of gravity leads only to minor changes in the results. In general, we find that the theoretical predictions for λ_m are in good quantitative agreement with the measured values of the drop distance for a wide range of α 's and A 's.

Acknowledgments: J.A.D and A.G.G. acknowledge support from Consejo Nacional de Investigaciones Científicas y Técnicas (CONICET, Argentina) and from Agencia Nacional de Promoción de Científica y Tecnológica (ANPCyT, Argentina) with grant PICT 2498/06. L.K. acknowledges partial support by the NSF Grant no. DMS-0908158.

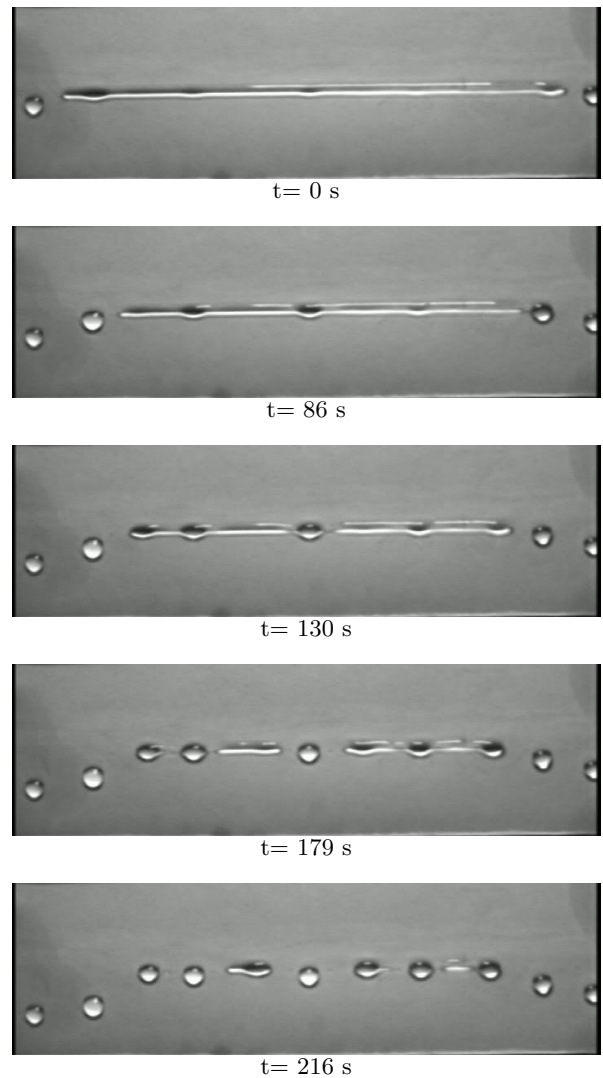


FIG. 26. Evolution of a PDMS rivulet with cross section $\tilde{A} = 0.0025 \text{ cm}^2 = 0.11a^2$. The inclination angle is $\alpha = 80^\circ$.

Appendix: Comparison with van der Waals model

It is of interest to compare the present results, obtained using a slip model, with those using other approaches to deal with the contact line divergence. A usual approach is based on the inclusion of liquid/solid interaction forces, such as those of van der Waals (vdW) type in the formulation of the problem (see, e.g. [1, 10, 31]). This inclusion can be accomplished by setting ℓ to zero in Eq. (26), and adding the term

$$K_{vw} \partial (h^3 f'(h) \partial h / \partial x),$$

on the left hand side. Here, $f(h)$ stands for the conjoining-disjoining pressure describing liquid/solid interaction through a vdW type of potential. Various models for this pressure term have been used; as an example

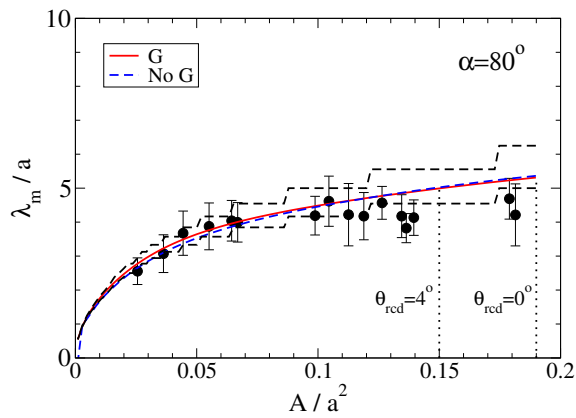


FIG. 27. Average spacing between drops (symbols) as a function of its cross section, A . The inclination angle is $\alpha = 80^\circ$. The curves correspond to λ_m as predicted by the LSA considering and neglecting gravity effects, and using $\ell = 10^{-3}$. The vertical dotted lines indicate A^* for $\theta_{rcd} = 0^\circ$ and 4° . The step-like dashed lines are illustrating finite-size effects, as discussed in the text.

here we consider a power law model [31]

$$f(h) = \left(\frac{h_*}{h}\right)^3 - \left(\frac{h_*}{h}\right)^2, \quad (\text{A.1})$$

where h_* is the equilibrium thickness of a flat film subject only to this pressure. Thus, it corresponds to the thickness of the film ahead of the contact lines, extending (mathematically) to infinity. The dimensionless constant in that term is

$$K_{vw} = \frac{2(1 - \cos \theta_0)}{h_*}. \quad (\text{A.2})$$

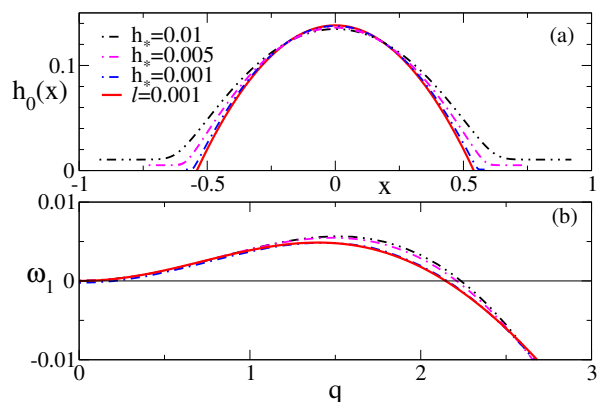


FIG. 28. Comparison between: (a) the thickness profiles and (b) the corresponding dispersion relations obtained with the slip method (solid line) and with disjoining pressure model (dashed lines) for different values of the equilibrium film thickness, h_* . The other parameters are as in Fig. 4.

Within the disjoining pressure model, only the horizontal substrate can support a static thickness profile, since an inclined plane unavoidably implies a small downward flow in the equilibrium film region. Therefore, strictly speaking, no static solution is admissible. For the horizontal case, where both models admit a static solution, we show in this Appendix that the results are in agreement if the thickness of equilibrium film is of the same order of magnitude as the slip length.

Figure 28 shows a comparison of the thickness profiles and the corresponding dispersion curves obtained using the slip model (solid lines), and disjoining pressure model for different h_* (dotted and dashed lines). As h_* decreases towards the value of $\ell (= 10^{-3})$, both the thickness profile and the dispersion curves tend to coincide. Thus, we can safely assume that both models are essentially equivalent for small values of their corresponding characteristic lengths, namely h_* and ℓ . Note, however, one difference: the marginal wavenumber depends (albeit weakly) on h_* in the disjoining pressure model, while it is independent of ℓ in the slip model.

For the inclined plane, we find that neither steady nor static solution with straight contact lines is possible within our simple vdW model, since different contact angles are required at both lines. Thus, one has two options: either $K_{vw} = \text{const.}$ and two different values of h_* at both contact lines are needed, leading to different macroscopic contact angles θ_r and θ_f , or $h_* = \text{const.}$ and two different values of K_{vw} are assumed. Possibly, a function $h_*(x)$ or $K_{vw}(x)$ could resolve this issue. On the other hand, due to the local character of the contact angles within the slip model, the slip length is independent of these angles. This fact allowed us to treat the present problem as discussed in the main text of the paper.

[1] A. Oron, S. H. Davis, and S. G. Bankoff. Long-scale evolution of thin liquid films. *Rev. Mod. Phys.*, 69:931, 1997.

[2] H. Huppert. Flow and instability of a viscous current down a slope. *Nature*, 300:427, 1982.

[3] S. M. Troian, E. Herbolzheimer, S. A. Safran, and J. F.

- Joanny. Fingering instabilities of driven spreading films. *Europhys. Lett.*, 10:25, 1989.
- [4] L. Kondic and J. Diez. Contact line instabilities of thin film flows: Constant flux configuration. *Phys. Fluids*, 13:3168, 2001.
- [5] J. Diez, A. G. González, J. Gomba, R. Gratton, and L. Kondic. Unstable spreading of a fluid filament on a vertical plane: Experiments and simulations. *Physica D*, 209:49, 2005.
- [6] K. Sekimoto, R. Oguma, and K. Kawasaki. Morphological stability analysis of partial wetting. *Annals of Phys.*, 176:359, 1987.
- [7] A. Münch and B. A. Wagner. Numerical and asymptotic results on the linear stability of a thin film spreading down a slope of small inclination. *Euro. J. of Appl. Math.*, 10:297, 1999.
- [8] K. Neuffer M. Bestehorn. Surface patterns of laterally extended thin liquid films in three dimensions. *Phys. Rev. Lett.*, 87:046101, 2001.
- [9] U. Thiele, K. Neuffer, M. Bestehorn, Y. Pomeau, and M. G. Velarde. Sliding drops on an inclined plane. *Colloids and Surfaces A*, 206:87, 2002.
- [10] U. Thiele and E. Knobloch. Front and back instability of a liquid film on a slightly inclined plane. *Phys. Fluids*, 15:892, 2003.
- [11] J.H. Snoeijer, B. Andreotti, G. Delon, and M. Fermigier. Relaxation of a dewetting contact line. Part 1. A full-scale hydrodynamic calculation. *Phys. Rev. Lett.*, 87:036102, 2001.
- [12] R. V. Craster and O. K. Matar. Dynamics and stability of thin liquid films. *Rev. Mod. Phys.*, 81:1131, 2009.
- [13] S. H. Davis. Moving contact lines and rivulet instabilities. Part i: The static rivulet. *J. Fluid. Mech.*, 98:225, 1980.
- [14] R. V. Roy and L. W. Schwartz. On the stability of liquid ridges. *J. Fluid. Mech.*, 391:293, 1999.
- [15] D. Langbein. The shape and stability of liquid menisci at solid edges. *J. Fluid. Mech.*, 213:251, 1990.
- [16] L. Yang and G. M. Homsy. Capillary instabilities of liquid films inside a wedge. *Phys. Fluids*, 19:044101, 2007.
- [17] J. Diez, A. G. González, and L. Kondic. On the breakup of fluid rivulets. *Phys. Fluids*, 21:082105, 2009.
- [18] A. G. González, J. Diez, R. Gratton, and J. Gomba. Rupture of a fluid strip under partial wetting conditions. *Europhys. Lett.*, 77:44001, 2007.
- [19] L. Kondic, J. Diez, P. Rack, Y. Guan, and J. Fowlkes. Nanoparticle assembly via the dewetting of patterned thin metal lines: Understanding the instability mechanism. *Phys. Rev. E*, 79:026302, 2009.
- [20] Y. Wu, J. D. Fowlkes, P. D. Rack, J. A. Diez, and L. Kondic. On the breakup of patterned nanoscale copper rings into droplets via pulsed-laser-induced dewetting: Competing liquid-phase instability and transport mechanisms. *Langmuir*, 26:11972, 2010.
- [21] Y. Wu, J.D. Fowlkes, N.A. Roberts, J.A. Diez, L. Kondic, A.G. Gonzalez, and P.D. Rack. Competing liquid phase instabilities during pulsed laser induced self-assembly of copper rings into ordered nanoparticle arrays on sio2. *Langmuir*, 27:13314, 2011.
- [22] J. D. Fowlkes, L. Kondic, J. Diez, and P. D. Rack. Self-assembly versus directed assembly of nanoparticles via pulsed laser induced dewetting of patterned metal films. *Nano Letters*, 11:2478, 2011.
- [23] L. M. Hocking and M. J. Miksis. Stability of a ridge of fluid. *J. Fluid. Mech.*, 247:157, 1993.
- [24] L. M. Hocking. Sliding and spreading of thin two-dimensional drops. *Q. J. Mech. Appl. Math.*, 34:37, 1981.
- [25] P. Roura and J. Fort. Equilibrium of drops on inclined hydrophilic surfaces. *Phys. Rev. E*, 64:011601, 2001.
- [26] B. Krasovitski and A. Marmur. Drops down the hill: theoretical study of limiting contact angles and the hysteresis range on a tilted plate. *Langmuir*, 21:3881, 2005.
- [27] E. B. Dussan V. The moving contact line: the slip boundary condition. *J. Fluid Mech.*, 77:665, 1976.
- [28] L. M. Hocking. Spreading and instability of a viscous fluid sheet. *J. Fluid. Mech.*, 221:373, 1990.
- [29] John P. Boyd. *Chebyshev and Fourier Spectral Methods*. Dover, New York, 2000.
- [30] T. Podgorski, J. M. Flesselles, and L. Limat. Corners, cusps, and pearls in running drops. *Phys. Rev. Lett.*, 87:036102, 2001.
- [31] J. Diez and L. Kondic. On the breakup of fluid films of finite and infinite extent. *Phys. Fluids*, 19:072107, 2007.